[Article ID] 1003- 6326(2002)04- 0734- 14

Effects of cyclic loading on temperature evolution of ULTIMET superalloy: experiment and theoretical modeling①

L. Jiang[1], H. Wang[2], P. K. Liaw[1], C. R. Brooks[1], D. L. Klarstrom[3]
(1. Department of Materials Science and Engineering, University of Tennessee, Knoxville, TN 37996, USA;
2. Metals and Ceramics Division, Oak Ridge National Laboratory, Oak Ridge, TN 37831, USA;
3. Haynes International Inc., Kokomo, IN 46904, USA)

[Abstract] High-speed, high-resolution infrared thermography, as a non-contact, full-field, and nondestructive technique, was used to study the temperature variations of a cobalt-based ULTIMET alloy subjected to cyclic fatigue. During each fatigue cycle, the temperature oscillations, which were due to the thermal-elastic-plastic effects, were observed and related to stress—strain analyses. The change of temperature during fatigue was utilized to reveal the accumulation of fatigue damage. A constitutive model was developed for predicting the thermal and mechanical responses of ULTIMET alloy subjected to cyclic deformation. The model was constructed in light of internal-state variables, which were developed to characterize the inelastic strain of the material during cyclic loading. The predicted stress—strain and temperature responses were found to be in good agreement with the experimental results.

[Key words] fatigue; thermography; temperature; constitutive model; NDE; superalloy
[CLC number] TG 146.1 [Document code] A

1 INTRODUCTION

It is well known that a material changes its temperature because of the mechanical deformation[1~11]. In materials subjected to cyclic loading, the dissipated mechanical energy can be characterized by hysteresis effects. Most of the energy manifests itself as heat. The temperature evolution, resulting from the heat generated during the fatigue process, was utilized to monitor the fatigue crack propagation[3~6], to measure the energy required to produce a unit area of a fatigue crack by propagation[7], to determine the endurance limit of some materials[8, 9], and to characterize the evolution of cumulative damage in the fatigue process[1, 2, 10, 11].

The temperature evolution is complicate, and the data are hard to interpret not only due to the interrelated effects of thermal and mechanical coupling, strain amplitudes, and loading histories, but also owing to multiple modes of heat transfer from the material to the environment. The generated heat is mainly removed from the material by three processes: 1) conduction, which is the transfer of heat along a solid object, 2) convection, which transfers heat through the exchange of hot and cold molecules, e. g., air, water, etc., and 3) radiation, which is the transfer of heat via electromagnetic (usually infrared) radiation.

In the present research, a state-of-the-art infrared (IR) thermography system was utilized to study temperature evolution of ULTIMET alloy, a cobalt-based superalloy, subjected to high-cycle and low-cycle fatigue at room temperature in air. A one-dimensional model was formulated to predict the thermal and mechanical responses of ULTIMET alloy undergoing cyclic fatigue. This model is based on the thermodynamics with internal-state variables originally reported by Coleman and Gurtin[12].

2 PHYSICAL BACKGROUND OF TEMPERATURE EVOLUTION

The thermal and mechanical coupling effect exists in metals during mechanical deformation. Considering a solid stressed in the elastic range under adiabatic conditions, the state of the solid can be described by the strain ε, (or stress, σ) and temperature (T). The equation of the state has the form:

$$f(\varepsilon, T) = 0 \text{ or } f(\sigma, T) = 0 \quad (1)$$

In the elastic-deformation range in which the Hooke's law applies, the stress (or strain)—temperature relation can be derived from the laws of thermodynamics[13]. The well-known thermoelastic effect can be described as

$$\Delta T = T - T_0 = -K\frac{ET}{1-2\upsilon}\Delta\varepsilon$$

or $$\Delta T = T - T_0 = -KT\Delta\sigma \quad (2)$$

where K is a material constant, $K = \frac{\bar{\alpha}}{\rho c_V}$, $\bar{\alpha}$ is the

① [Received date] 2001- 10- 08

coefficient of linear thermal expansion, ρ is the mass density, c_V is the specific heat at a constant volume, ΔT is the change of the absolute temperature, T is the absolute temperature of the current state, T_0 is the absolute temperature of the previous state, $\Delta\varepsilon$ is the change of strain, $\Delta\sigma$ is the change of stress, and υ is Poisson's ratio.

In Eqn. (2), the temperature variation is negatively proportional to a change in the stress or strain states of a homogenous elastic solid. In other words, the temperature decreases as the stress or strain increases in the elastic range, and vice versa. Based on the thermoelastic effect, a great deal of research has been done on the stress pattern analysis by the characteristic evolution of temperature under either adiabatic or non-adiabatic conditions[13~15].

Fatigue of materials, as a complicate process of gradual accumulation of damage, is mainly controlled by the amplitude of the plastic deformation[16, 17]. It is well known that the stored energy is generally only a small portion of the energy dissipated during fatigue[18~20]. Even during the fatigue crack propagation process, the stored energy, which is the integration of the increase of internal energy over all the elements in the plastic zone, is very small, compared with the dissipation of mechanical energy, which can be measured from the stress—strain hysteresis loop[19, 20]. Especially, high cyclic stresses or large cyclic plastic strain is the predominant cause of energy dissipation. The conversion of the mechanical energy into heat may be significant, and may have considerable effects on the fatigue behavior.

In the plastic deformation range, the stress and strain relation is nonlinear. The strain cannot be completely recovered. For constitutive modeling, the present state of a material depends upon either the present values and the past history of the observable state variables only, leading to hereditary theories, or the present values of both observable state variables and a set of internal-state variables, which are not directly observable. Based on these two assumptions, the functional theory and internal state variable theory are developed. The internal-state-variable approach is very attractive for modeling the nonlinear behavior of crystalline solids.

In recent years, there was a substantial development of so-called "Unified theories", in which the irreversible processes, such as inelastic behavior and damage, were represented by a set of internal variables[21]. Kratochvil and Dillon[22~24] presented an analytical framework for the study of crystalline elastic-plastic materials and elastic-visco-plastic materials in the thermal and mechanical fields. Krempl, et al[25~28] proposed a rate-dependent isotropic theory, and the mechanical constitutive equation and the heat-conduction equation were developed. Moreover, Allen et al[29, 30] formulated a thermodynamic model to predict the thermomechanical responses in a thermoviscoplastic uniaxial bar using internal state variables. Hart[31] proposed internal state variables based on the consideration of micromechanisms of material deformation, e.g., grain boundary sliding. Although those intended plasticity theories differed in the choice of hardening variables, those models were represented in a unified way as internal state variables.

To describe the heat-evolution phenomenon of an elastic-plastic material during cyclic fatigue, a thermodynamics-based framework may be developed with internal state variables. Herein, only thermal and mechanical properties of an isotropic material are considered, and magnetic, electric, and other factors are neglected. Most of all, the irreversible deformation behavior is described by a set of internal state variables, which can characterize the state of the elastic-plastic deformation of a solid. All the mechanical, thermodynamic, and internal-state variables are referred to a rectangular Cartesian system with the axes, x_j, where j takes on the values of 1, 2, and 3. The time is designated as t. Thus, all the state variables described herein are functions of x_j and t.

The discussion is limited to the case of infinitesimal deformation, and the initial state is assumed to be stress-free. The present state of the material is characterized by the independent observable state variables, including a total strain, ε (or stress, σ), absolute temperature, T, temperature gradient, ΔT, and internal state variables, α_i, where i is the number of internal variables ranging from 1 to n. The internal-state variables are assumed to be sufficient for characterizing the state of inelastic deformation of a solid. The state of the solid may be described as

$$f(\varepsilon, \alpha_i, \Delta T, T) = 0$$

or

$$f(\sigma, \alpha_i, \Delta T, T) = 0 \tag{3}$$

The total strain is assumed to be composed of the elastic strain, ε_E, and the inelastic strain, ε_I, which can be represented by internal state variables, α_i.

$$\varepsilon = \varepsilon_E + \varepsilon_I = \varepsilon_E + \alpha_i \tag{4}$$

where the summation on the range of i is implied. The state of the material must satisfy the first law of thermodynamics, i.e., the conservation of energy. The thermodynamic first law may be described as

$$\rho\frac{\mathrm{d}U}{\mathrm{d}t} - \sigma\frac{\mathrm{d}\varepsilon}{\mathrm{d}t} + \Delta q = \rho r \tag{5}$$

where ρ is the mass density, U is the internal energy per unit mass, q is the heat flux, and r is the heat supply per unit mass. On the left-hand side of Eqn. (5), the first term is the change of internal energy, the second term is the input of mechanical energy, and the third term is the heat conduction. The right-hand side of Eqn. (5) is the heat supply by internal sources.

The volumetric Helmholtz free energy, H, is selected as the thermodynamic potential throughout, as

$$H = U - TS \quad (6)$$

where S is the entropy per unit mass.

For a thermodynamic process, e. g., fatigue, the second principle of thermodynamics asserts an increment of entropy, $\Delta S > 0$. In a variational form, the Clausius-Duhem inequality states that the rate of production of entropy per unit mass, γ, is not negative:

$$\rho\gamma = \rho\frac{\mathrm{d}S}{\mathrm{d}t} - \left[\frac{\Theta}{T} - \Delta\left(\frac{q}{T}\right)\right] \geqslant 0 \quad (7)$$

In addition, for one-dimensional heat conduction, the heat flux can be described by Fourier's equation

$$q = -k\Delta T \quad (8)$$

where k is the thermal conductivity, and is assumed to be a constant.

Following the classical approach of Coleman and Gurtin[12], the coupled thermal-mechanical equation is derived as

$$\rho\frac{\partial H}{\partial \alpha_i}\frac{\mathrm{d}\alpha_i}{\mathrm{d}t} - \rho T\frac{\partial^2 H}{\partial \alpha_i \partial T}\frac{\mathrm{d}\alpha_i}{\mathrm{d}t} - \rho T\frac{\partial^2 H}{\partial \varepsilon \partial T}\frac{\mathrm{d}\varepsilon}{\mathrm{d}t} - \rho T\frac{\partial^2 H}{\partial T^2}\frac{\mathrm{d}T}{\mathrm{d}t} - k\Delta q = \Theta \quad (9)$$

It can be seen from Eqn. (9) that the temperature, total strain, and inelastic strain are correlated through the Helmholtz free energy. In addition, all the above equations and discussions can be equivalently transformed in terms of the Gibbs free energy. The proper choices of internal-state variables and the formulation of the Helmholtz free energy based on the experimental justifications are crucial for the prediction of the thermal and mechanical responses of a material subjected to cyclic fatigue.

3 EXPERIMENTAL

3.1 Material

ULTIMET alloy, developed by Haynes International, Inc., is a Co-Cr alloy containing mainly about 26% Cr (mass fraction). The nominal chemical composition is shown in Table 1. The material used for high-cycle fatigue testing was produced as follows: a plate feedstock was reduced in thickness from 30.48 cm to 1.27 cm in a 4-pass cross-rolling sequence at 1 200 ℃, and then, the material was solution-annealed at 1 120 ℃ for about 20 to 30 min and water-quenched to room temperature in order to retain the face-centered-cubic (FCC) structure. At room temperature, the average yield strength of the alloy, which was defined at the intersection of the monotonic stress—strain curve and the 0.2% offset line, was 586 MPa. The tensile strength, which was defined as the maximum load divided by the initial cross-sectional area, was 1 GPa. The elongation was 39% with a gage length of 19.05 mm.

3.2 Fatigue testing

A newly-developed electrohydraulic material test system was used for the fatigue experiments. This material test system featured an MTS Teststar IIs controller and operation software, which allowed customized configurations to satisfy different requirements for mechanical testing. It had high-accuracy data-control and fast data-acquisition capabilities. The extensometer used was capable of measuring strains during a fatigue test with a frequency ranging from 0 to 100 Hz. The traveling distance of the extensometer was 1.27 mm with a gage length of 12.7 mm. All the tests were conducted in air at ambient temperature (about 298 K).

Table 1 Nominal chemical composition (mass fraction, %)

Co	Cr	Ni	Mo	W
Bal.	29	9	5	2
Fe	Mn	Si	N	C
3	0.8	0.3	0.08	0.06

Uniaxial high-cycle fatigue tests were performed using cylindrical specimens. The geometry of the specimen is shown in Fig. 1. The gage section featured a diameter of 5.08 mm and a length of 19.05 mm. The fatigue-test procedures were in accordance with the American Society for Testing and Materials (ASTM) standard E466 for "Conducting Constant Amplitude Axial Fatigue Tests of Metallic Materials"[32]. High-cycle fatigue tests were conducted under load control using a sinusoidal waveform at 20 Hz. Loading was from tension to tension, with a R ratio ($\sigma_{min}/\sigma_{max}$, where σ_{min} and σ_{max} were the minimum and maximum applied stresses, respectively) of 0.05. High-cycle fatigue tests were performed until the failure of a specimen or up to approximately 10^7 cycles as run-out.

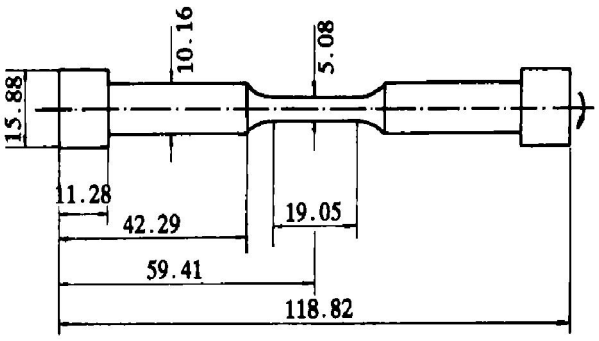

Fig. 1 Specimen geometry for high-cycle fatigue

3.3 IR thermography

Infrared is an invisible portion of the light spectrum extending from 0.75 to 1 000 μm. All objects warmer than absolute zero Kelvin emit energy somewhere within that range. The IR thermography is a process of detecting the invisible infrared radiation and converting the energy detected into visible light.

The resultant image depicts and quantifies the energy being radiated and reflected from the object viewed, and can be transformed into temperature maps. The IR thermography is a convenient technique for developing digital temperature maps from the invisible radiant energy emitted from stationary or moving objects at any distance. There is no surface contact or any perturbation of the actual surface temperature of the objects investigated. In the present study, a state-of-the-art, high-speed, and high-sensitivity Raytheon Radiance HS infrared imaging system was used to record the temperature changes during high-cycle and low-cycle fatigue. The IR camera had a 256 mm × 256 mm pixels focal-plane-array (FPA) InSb detector, which was sensitive to 3~ 5 μm wavelength thermal radiation. The camera could be operated in a snapshot mode and could be externally triggered. In the high-speed mode, i. e., 144 Hz, up to 800 full-frame images could be taken into the memory of the frame-grab card, and then, transferred into the hard disk. In the low-speed mode, i. e., 2 Hz or slower, 1, 000 full-frame images (about 100 MB) or more could be stored directly into the hard disk. The temperature resolution of the camera was 0. 015 K at 298 K. In addition, the IR imaging system was coupled with the material test system through a synchronizer to trigger the IR camera to record data at a certain stress level such that any phase lag of data recording was avoided.

Before fatigue testing, a thin submicroscopic graphite coating was applied to the specimen in order to reduce IR reflections and increase the thermal emissivity of the specimen surface. The relationship between the IR radiant energy and temperature was established by coupling the IR camera and a thermocouple. After a specimen with graphite coating was inserted into the material testing frame, a thermocouple was attached on the back of the specimen, and the IR camera was focused on the front surface. The specimen was heated up to a temperature greater than the estimated highest temperature during a fatigue test, and then, the specimen cooled down to the room temperature without perturbation. During the cooling period, the readout of the thermocouple and the thermographic image of the IR camera of the specimen were recorded simultaneously at a constant temperature interval, i. e., 5 K, until the temperature reached room temperature. Through the above calibration procedure, the relationship between the IR radiant energy and temperature was represented by a best-fit line based on the linear regression analysis of the measured values.

4 FATIGUE

4.1 Temperature evolution

The high-speed and high-resolution IR camera had the advantages to take a series of in-sequence snapshots at a frequency ranging from 0 to 144 Hz. The thermographic images produced were converted into a digitized-temperature-mapping file. With each thermographic image, the temperature distribution could be observed. With a set of images in sequence, the temperature evolution could be obtained for each pixel on the surface monitored. Detailed temperature distributions on the specimen surface and temperature changes as a function of time (cycles) could be utilized to characterize the fatigue process.

The spatial resolution of the IR camera was dependent on the focal distance of its optical lens. In the present study, the IR camera was kept at a relatively constant distance of about 200 mm from the specimen in order to monitor the whole gage section of the specimen and the shoulder section connecting the grip and gage sections. The area of a pixel represented 0. 149 mm × 0. 149 mm of the real dimension. A thermocouple attached on the back surface of the specimen was used for calibrating temperature and monitoring approximate temperature variations.

A typical thermographic image is shown in Fig. 2 (a). The brightness of color indicates the temperature difference. The brighter the color, the higher the temperature, as represented by the calibrated color bar of Fig. 2(a). From Fig. 2(a), a detailed temperature distribution could be obtained for the shoulder and gage sections of a specimen subjected to high-cycle fatigue.

With the aid of the high-speed mode of the IR camera, the detailed temperature evolution during high-cycle fatigue could be observed. Through the manipulation of thermographic images, the temperature changes along the centerline of the specimen, as indicated by a dash line in Fig. 2(a), could be obtained for a fatigue test. The total length of the shoulder and gage sections was about 34 mm. The IR camera was operated at 120 Hz, i. e., 120 full-frame images per second. The fatigue test was conducted at 20 Hz. The numbers 1 to 9, as shown in Fig. 2(b), indicate the data points acquired by the IR camera at a constant time interval of 1/120 s. These data points could equivalently represent time.

For the first fatigue cycle, the temperature oscillation along the centerline as a function of time and distance is presented in a three-dimensional graph (Fig. 2(b)). At both ends of the specimen-shoulder sections, the temperatures were relatively stable and kept at approximately 296. 4 K, which was close to the room temperature. However, the temperature varied greatly within the gage section. This was because the plastic strain (or strain) was mainly concentrated in the gage section. The temperature of the shoulder sections did not change very much because the stresses there were small and in the elastic region. In addition, during this very short period of time, heat transfer did not take place extensively.

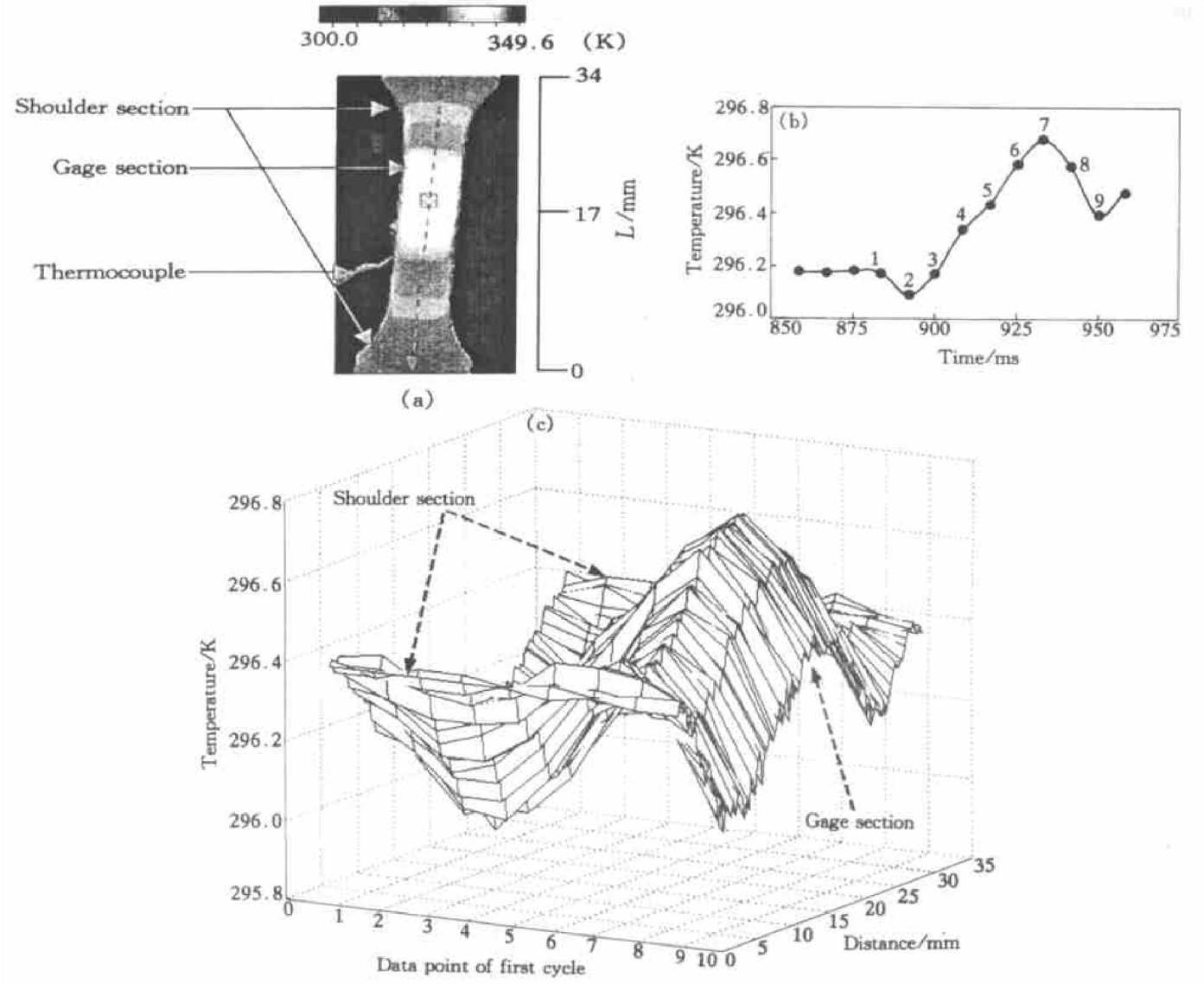

Fig. 2 Temperature variations along longitudinal direction of specimen during first cycle of fatigue experiment

(a) —Schematic presentation of centerline along specimen;

(b) —Three-dimensional temperature variations as function of time and distance;

(c) —Temperature evolution curve for midpoint of specimen (σ_{max} = 762 MPa, R = 0.05, room temperature, in air, fatigue life of 41024 cycles and 20 Hz)

Due to the specimen geometry, the plastic strain was concentrated at the specimen-gage section. Although there were conduction, convection, and radiation heat transfers occurring simultaneously, the heat generated in the material was mainly conducted through the axial direction of the specimen. Hence, the highest temperature was typically located at the midpoint of the specimen-gage section. To decrease the systematic error of the IR camera, the temperature of the midpoint was taken as an average temperature over 10 × 10 pixels domain around the midpoint, which is about 1.49 mm × 1.49 mm of real dimension, as shown schematically by the box in Fig. 2(a). Herein, the term "temperature" referred to the average temperature over the 10 × 10 pixels domain around the midpoint of a specimen.

Fig. 2(c) shows the temperature evolution curve for the midpoint of the specimen during the first fatigue cycle. The numbers 1 to 9 indicate the data points acquired by the IR camera at a constant time interval of 1/120 s. The temperature initially decreased from point 1 to 2, and then, increased from point 2 to 7 during the first cycle. In the second cycle, the temperature decreased from point 7 to 9. Thereafter, the cyclic pattern of the temperature repeated throughout the fatigue test. From Fig. 2, it can be seen that the IR camera was readily to detect the delicate temperature change, e.g., 0.1 K.

When the IR camera was operated at a lower frequency, e.g. 1/8 Hz, the overall trend of the temperature evolution could be observed. Herein, the term "mean temperature" referred to the temperature at the midpoint of the specimen gage section, which was acquired at a lower IR camera speed and was used for the representation of the average temperature over the time interval. Fig. 3 shows the mean temperature

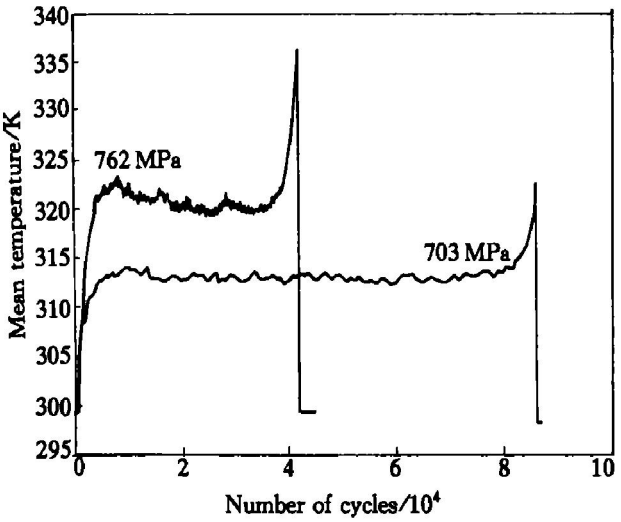

Fig. 3 Mean temperature profiles of ULTIMET alloy
(σ_{max} = 703 MPa and 762 MPa, R = 0.05, room temperature, in air, and 20 Hz)

profiles for fatigue tests at two maximum stress levels, 703 and 762 MPa. For the mean temperature profile at a maximum applied stress level of 703 MPa, the mean temperature initially rose from room temperature, 299 K, at the beginning, to 313.5 K at 9 000 cycles. The mean temperature stabilized at a steady state of around 313.5 K from 9 000 cycles to 80 000 cycles. Then, the mean temperature increased continuously until the specimen failed at a mean temperature of 323 K. With a maximum applied stress level of 762 MPa, the mean temperature rose from 299 K up to 323 K at 8 400 cycles, then remained at about 320 K to about 36 000 cycles. It then increased again until the specimen failed at a mean temperature of 336.5 K. It was observed that the mean temperature evolution during high-cycle fatigue underwent four stages: an initial increase, a steady state, an abrupt increase, and a final drop[1, 2]. For the same experimental conditions, a higher maximum stress level caused a higher steady-state mean temperature during fatigue tests, as illustrated in Fig. 3.

At an IR camera speed of 120 Hz, the temperature evolution curves for three maximum applied stress levels are shown in Fig. 4. At a maximum applied stress level of 645 MPa, the temperature oscillated within 0.5 K during the initial stage of the fatigue test, i.e., from 1 to 3 s. The average temperature, which is defined as the sum of temperature acquired in each cycle over the number of data points, increased slightly. At 703 MPa, the temperature exhibited the same oscillation phenomenon, but the average temperature had a noticeable increase of about 3.2 K during the first 2 s. At 762 MPa, the average temperature increased much higher to about 9.0 K. Generally, the temperature oscillated with a certain amplitude, and the average temperature increased with fatigue time. The amplitude of the temperature oscillation and the increase of the average temperature

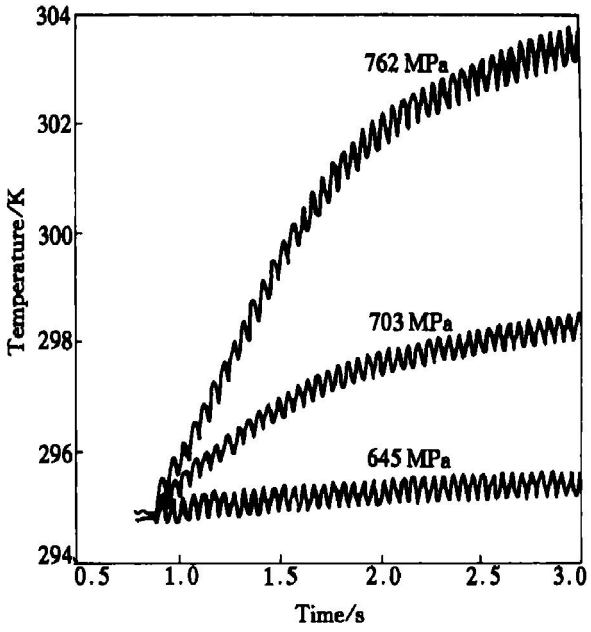

Fig. 4 Temperature evolution curves of ULTMET alloy
(σ_{max} = 645, 703 and 762 MPa, R = 0.05, room temperature, in air, and 20 Hz)

were found to increase with the maximum applied stress. The average temperature increased up to a constant level as the cycling continued, if the surrounding temperature did not change.

4.2 Mechanistic understanding

Throughout the experiments, the temperature of the specimen was recorded by the IR thermography system, and the stress—strain responses were documented by the MTS system. Using the system control, the load was increased to the mean load level and held for a short duration. Subsequently, a cyclic load with a maximum stress of 703 MPa was applied, as shown in Fig. 5(a). The corresponding evolution of strain and temperature within each fatigue cycle during initial loading are presented in Figs. 5(b) and (c). In the very short initial loading period of about 1 s, the load was applied relatively fast, and the condition of the specimen could be considered to be adiabatic. Note that the temperature evolution in Fig. 5 (c) was measured at a high IR camera speed of 120 Hz.

When the load was initially applied, the strain was elastic, and the stress (or strain) —temperature relation could be described by Eqn. (2). At the initial stress-free stage, the temperature was 295.60 K, but the temperature dropped to 295.27 K when the stress increased from 0 MPa to a mean stress level, 386 MPa, owing to the thermoelastic effect, as shown in Fig. 5. During the initial short holding time with the mean stress level of 368 MPa, as presented in Fig. 5 (a), the strain remained constant at 0.16% as exhibited in Fig. 5(b), and the temperature remained at 295.27 K without any obvious heat loss, as indicated in Fig. 5(c).

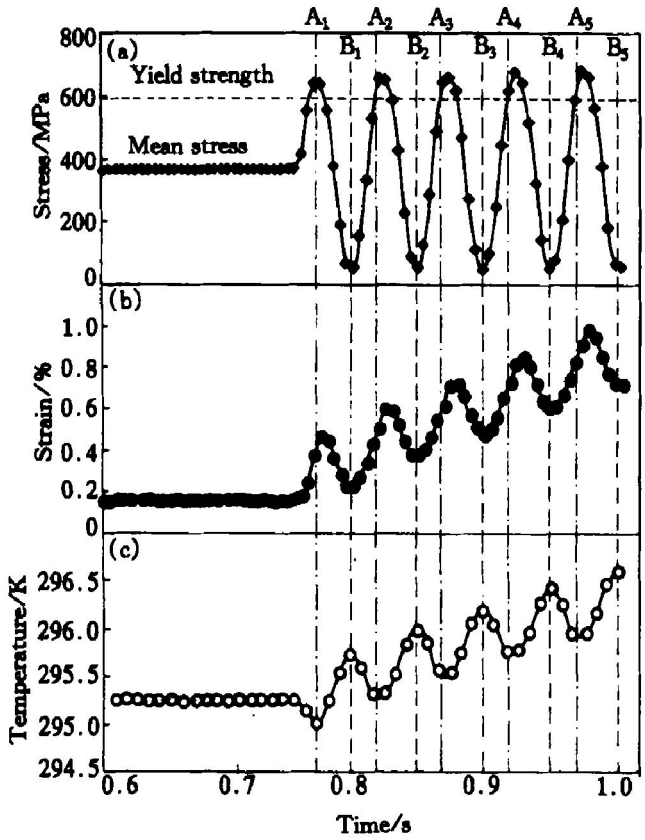

Fig. 5 Typical material responses of ULTIMET alloy during high-cycle fatigue test
(a) —Stress; (b) —Strain;
(c) —Temperature evolution versus time

As the stress and strain were continuously increased, the temperature decreased from 295.27 K to 295.02 K. After the stress reached the yield strength level of 586 MPa, the temperature started to increase because of the heat dissipation due to the irreversible plastic deformation beyond yielding. During the unloading cycle, the strain decreased, and the temperature continued to increase. For subsequent cycles, the strain and temperature responses repeated, but the residual level of plastic strain grew, and the mean temperature continuously increased. As indicated by the dash lines (B_1, B_2, B_3, B_4, and B_5) in Fig. 5, it is very clear that the temperature reached its highest point in each cycle when the stress and strain were at their minimums. However, when the temperature reached its cyclic minimum, the stress and strain were not at their maximam, as noted by the dash-dot lines (A_1, A_2, A_3, A_4, and A_5) in Fig. 5. This was because plastic yielding occurred prior to reaching the maximum stress, which initiated the temperature rise [Figs. 5(a) and (c)]. Thus, in the fatigue process, the thermoelastic effect caused the temperature to oscillate, and the irreversible inelastic deformation caused the mean temperature to increase. The temperature was found to oscillate within a range of approximately 0.4 K (as shown in Fig. 5), which was easily detected by the high-speed, high-resolution IR camera.

Typical stress—strain curves during initial cycling are presented in Fig. 6. Plastic deformation resulted because the maximum applied stress level was set at 703 MPa, 120% of yield strength of ULTIMET superalloy. It can be seen that the hysteresis loop was "walking", which is generally known as "cyclically creeping" or "ratcheting", in the direction of increasing tensile strains. It is also seen that, in Fig. 6(a), the hysteresis loop was not closed at the beginning of the high-cycle fatigue process. This was because the amount of plasticity in tension was not opposed by an equal amount of the plastic flow in compression. Hence, the cyclic ratcheting resulted, as illustrated in Fig. 6(a). At the beginning of cyclic loading, the area under the hysteresis loop was relatively large. The rate of ratcheting generally decreased as fatigue loading continued. As shown in Fig. 6(b), the differences between the hysteresis loops at the 252nd and 253rd fatigue cycles were not distinguishable. There was still a large amount of plastic strain buildup, which can be seen by comparing the relative positions of the hysteresis loops at the 252nd (or 253rd) and 370th cycles. The accumulation of the irreversible plastic strain continued until the mean strain reached a certain value depending up-

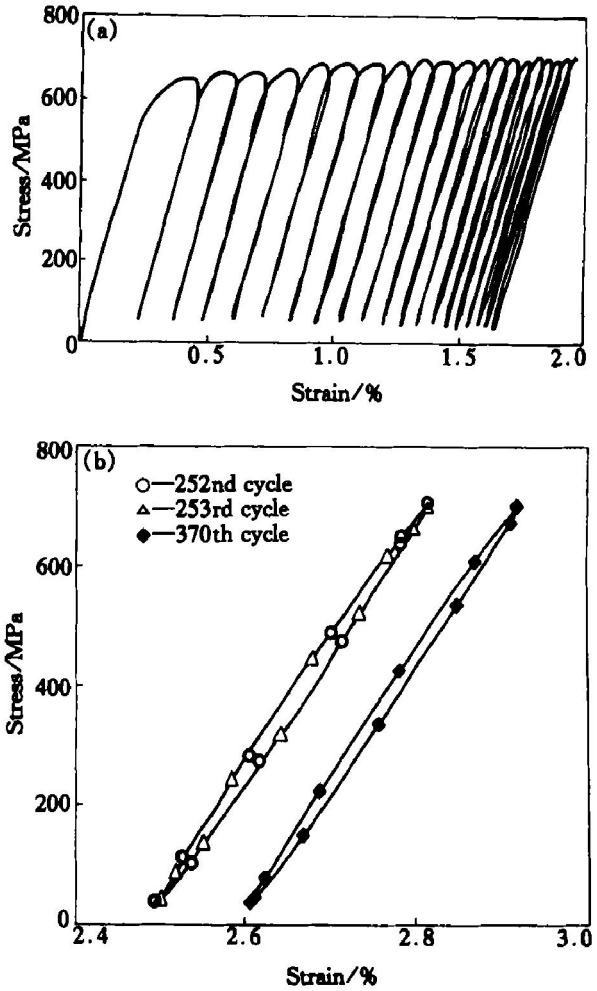

Fig. 6 Stress—strain curves
(a) —At beginning; (b) —at 252nd, 253rd, and 370 th cycles of fatigue test
(σ_{max} = 703 MPa, R = 0.05, room temperature, in air, fatigue life of 97 542 cycles and 20 Hz)

on the maximum stress level. Generally, within the stress range of 600 MPa to 764 MPa examined, the mean tensile strain eventually stabilized at a constant value after approximately 8 000 cycles, and the hysteresis loop remained constant. The stabilized mean strain and the area of the hysteresis loop increased as the maximum stress level was increased.

Above a certain cyclic stress sensitivity limit, the damping energy increased rapidly with the stress because the cyclic plastic strain began to be an important cause of energy dissipation. At high cyclic stresses, the plastic strain was the predominant source of energy dissipation. In the tension-tension, high-cycle fatigue test, the temperature evolution corresponded to the change of the stress—strain state. The temperature responded sensitively to the variation of the mechanical state. It was experimentally found that the stored energy was only a small amount of dissipated energy, < 1%[18]. Hence, almost all the irreversible mechanical energy due to the inelastic deformation could be converted into heat. The mechanical energy dissipated in each cycle could be represented by the area of the hysteresis loop, as shown in Fig. 6. It was very clear that during the initial cycles, the area of the hysteresis loop was much greater than it was for much later cycles. As the fatigue process continued, the accumulation of plastic strain in each cycle decreased due to strain hardening.

The increase of the mean temperature was proportional to the area of hysteresis loop. From the first law of thermodynamics, conservation of energy, assuming the specimen stressed in an adiabatic condition, and ignoring the energy stored inside the material, is

$$\rho c_V \Delta T = \int_{\varepsilon_1}^{\varepsilon_2} \sigma_u \mathrm{d}\varepsilon - \int_{\varepsilon_1}^{\varepsilon_2} \sigma_l \mathrm{d}\varepsilon \qquad (10)$$

where ε_1 and ε_2 are the minimum and maximum strains, respectively, of the hysteresis loop, and σ_u and σ_l refer to the local stresses in the upper and lower curves of the hysteresis loop. For ULTIMET alloy, ρ is 8 470 kg/m^3, and c_V is approximately equal to the specific heat at a constant pressure, 456 J/(kg·K)[33]. Using the digitized stress—strain data, as shown in Fig. 6, the calculated maximum temperature for each cycle using Eqn. (10) is shown in Fig. 7. It can be seen that for the initial cycles, the predicted maximum temperature matched the experimental data quite well, after which deviations occurred. The reason why this trend occurred was that during the initial cycling, the condition of the specimen was essentially adiabatic because of the fast loading condition. After that, heat-transfer effects became important. Therefore, the predicted maximum temperature at greater fatigue cycles (longer time) was higher because heat conduction had not been considered in the calculation.

As stated in Eqn. (10), the increase of the mean temperature is proportional to the area of the hysteresis loop. In Figs. 6 and 7, initially the increase of the mean temperature was relatively high due to the large plastic deformation. As shown in Fig. 7, however, the increase of the mean temperature decreased as the fatigue process progressed due to the decreasing plastic stain (as shown in Fig. 6), and the increasing heat-transfer effects.

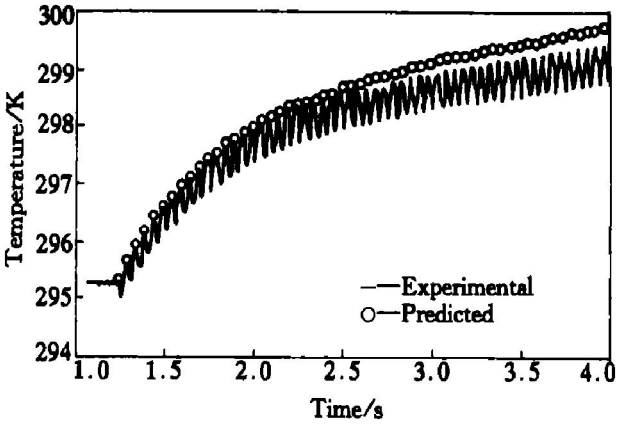

Fig. 7 Calculated and measured temperature evolution during high-cycle fatigue
(σ_{max} = 703 MPa, R = 0.05, room temperature, in air, fatigue life of 97 542 cycles and 20 Hz)

4.3 Temperature profile during high-cycle fatigue

The thermal and mechanical responses of ULTIMET superalloy are summarized in Fig. 8, which includes both the mean temperature and displacement evolution of the material during high-cycle fatigue under load control. The maximum and minimum displacements followed the same trend as the mean temperature. Initially, the displacement increased due to the uniformly distributed plastic deformation of the specimen gage section. It was known that slip lines generally multiplied and grew into persistent slip bands (PSB). PSBs carried essentially all of the plastic strain in the low-amplitude fatigue

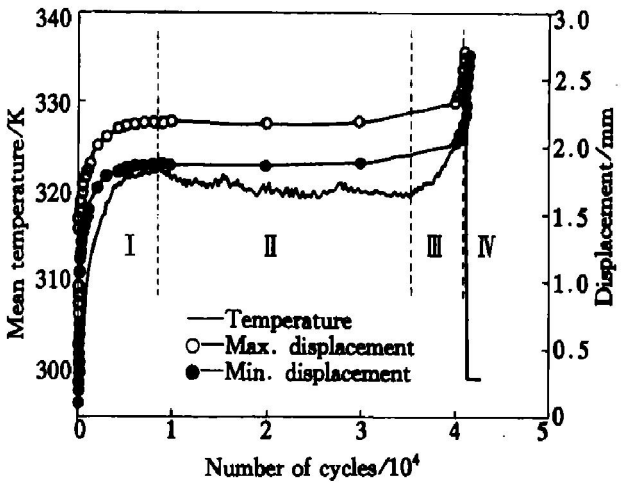

Fig. 8 Mean temperature and displacement evolution of specimen during high-cycle fatigue
(σ_{max} = 762 MPa, R = 0.05, room temperature, in air, fatigue life of 41 024 cycles and 20 Hz)

tests[8, 34]. In the initial stage, the increase in temperature can be associated with plastic deformation. In the second stage, the maximum and minimum displacements remained essentially constant. With the formation of persistent slip bands, which were distributed regularly over the gage section, the stress and strain responses were stabilized as illustrated by the closed hysteresis loop in Fig. 6(b). The stabilized stress—strain curve resulted in a steady-state mean temperature.

Once a macrocrack formed, the steady-state stress—strain responses collapsed, and the third stage emerged. In the third stage, the displacement increased again. Macrocracks caused extensive plastic deformation at the crack tip. Hence, the steady state of the mean temperature was disrupted, and the mean temperature exhibits another rise. The propagation of a macrocrack could eventually lead to the failure or separation of the specimen, and a corresponding drop of the mean temperature in the fourth stage.

In summary, the temperature evolution during high-cycle fatigue was related to the stress—strain state and fatigue damage. The mean temperature profile of a high-cycle fatigue test typically exhibits four stages: 1) an initial raise due to the heat generation resulting from irreversible deformation of the material; 2) a steady state resulting from a balance between heat generation and heat conduction in the material; 3) an abrupt increase (the breakdown of the steady state) owing to the large plastic deformation caused by stress concentration at the crack tip; and 4) a final drop, caused by the separation of the test specimen.

5 THEORETICAL MODELING

5.1 Characteristic constitutive equations for cyclic fatigue

The present model is restricted to the consideration of an isotropic, long, and slender bar, which is subjected to a homogeneously applied deformation field, such that the resulting stress field is everywhere uniaxial in one dimension. All the mechanical, thermodynamic, and internal state variables are referred to a one-dimensional system with the axis, x, which is along the longitudinal direction of the cylindrical specimen. When $x = 0$, it corresponds to the midpoint of the gage section of the specimen. Thus, all the state variables described herein are functions of x and t. The boundary conditions are shown in Fig. 9, and there is no internal heat source, i.e., $r = 0$ in Eqn. (9). With the consideration of one dimension, the convection and radiation around longitudinal boundaries can be incorporated into Eqn. (9) as

$$\rho\frac{\partial H}{\partial \alpha_i}\frac{\mathrm{d}\alpha_i}{\mathrm{d}t} - \rho T\frac{\partial^2 H}{\partial \alpha_i \partial T}\frac{\mathrm{d}\alpha_i}{\mathrm{d}t} - \rho T\frac{\partial^2 H}{\partial \varepsilon \partial T}\frac{\mathrm{d}\varepsilon}{\mathrm{d}t} - \rho T\frac{\partial^2 H}{\partial T^2}\frac{\mathrm{d}T}{\mathrm{d}t} - k\frac{\partial^2 T}{\partial x^2} + h\frac{p}{A}(T - T_r) + \frac{p}{A}GFs(T^4 - T_r^4) = 0 \quad (11)$$

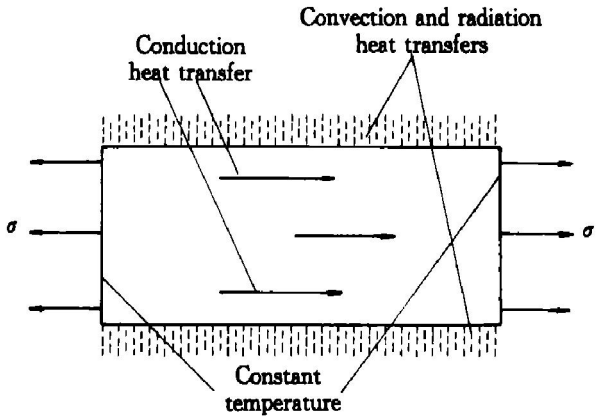

Fig. 9 Sketch showing boundaries conditions of ULTIMET alloy during fatigue

where h is the convection heat transfer coefficient, p is the circumference of the cylindrical bar, A is the cross-sectional area of the cylindrical bar, T_r is the temperature of environment, G is the geometric factor between the specimen and surroundings, $F(\leqslant 1)$ is the factor termed the emissivity, and s is the Stefan-Boltzmann constant. On the left-hand side of Eqn. (11), the first three terms are related to the change of a mechanical state, the fourth term is the accumulation of temperature, the fifth term is the heat conduction, the sixth term is the heat convection, and the seventh term is the heat radiation. Eqn. (11) is the governing equation describing the thermal and mechanical responses of a material subjected to cyclic fatigue.

Bonder and Partom[35, 36] postulated a model based on two internal state variables, which were referred to hardness variables. One was related to the isotropic hardening, and the other was the variable accounting for the directional character of resistance to the plastic flow following deformation. The Bonder and Partom model was employed to characterize the constitutive response of various materials, e.g., nickel-based alloys[37~40], aluminum alloys[39], solder materials[40], and some other materials, e.g. copper and titanium[35, 36]. The internal state variable, α_1, can be represented by the kinetic equation[35~41]:

$$\frac{\mathrm{d}\alpha_i}{\mathrm{d}t} = \frac{2}{\sqrt{3}}D_0\exp\left[-\left(\frac{1}{2}\right)\left(\frac{Z}{\sigma}\right)^{2n}\right] \quad (12)$$

where D_0 and n are experimentally obtained material constants, and Z is a measure of the strain hardening, which is a function of the plastic work.

Z is composed of isotropic and kinematic hardening,

$$Z = Z_I + Z_D \quad (13)$$

where Z_I is the isotropic variable, and Z_D is the directional hardening variable.

The evolution equations for the isotropic and the directional hardening variables without thermal recovery are described by Eqn. (14) and (15), respective-

ly:

$$\frac{dZ_1}{dt} = m_1(Z_1 - Z_I)\frac{dW_p}{dt};\ Z_I(0) = Z_0 \quad (14)$$

$$\frac{dZ_D}{dt} = \frac{m_2}{2}[1 + \exp(-m_3 Z_D)](Z_2 - Z_D)\frac{dW_p}{dt};\ Z_D(0) = Z_0 \quad (15)$$

where m_1, m_2, m_3, Z_1, Z_2, and Z_0 are material constants. m_1, m_2, m_3, Z_1, and Z_2 are strain rate and temperature independent for the material modeling purpose. Z_0 is strain-rate independent, but temperature dependent. In addition, the plastic work, W_p, is determined by

$$\frac{dW_p}{dt} = \sigma\frac{d\alpha_1}{dt} \quad (16)$$

Following Allen's postulation[30], the Helmholtz free energy is expanded in the form of Taylor's series in terms of the elastic strain and temperature as

$$H = H_0 + \frac{E_e}{2\rho}\varepsilon_E^2 - \frac{c_V}{2T_0}\Delta T^2 \quad (17)$$

where H_0 is the free energy in the initial state, a constant, E_e, is the effective elastic modulus, which takes into account of the fatigue damage, and ΔT is the temperature difference between the current temperature, T, and the initial temperature, T_0, at the strain-free state, $\Delta T = T - T_0$. The specific heat at a constant volume, c_V, is

$$c_V = -T\frac{\partial^2 H}{\partial T^2} \quad (18)$$

Note that in Eqn. (17), although the first-order terms have been neglected, the coupling among the total strain, inelastic strain, and temperature is retained[30]. Note also that the energy dissipation due to microstructural changes has been neglected in the free-energy Eqn. (17), because this mechanism was shown to contribute only a small portion of energy to the dissipation process[20, 30]. Further, the fracture energy loss resulting from the crack propagation is neglected.

With the consideration of thermal expansion and Eqn. (4), the elastic strain can be described as

$$\varepsilon_E = \varepsilon - \varepsilon_I = \varepsilon - \alpha_1 - \bar{\alpha}\Delta T \quad (19)$$

where $\bar{\alpha}$ is the thermal expansion coefficient. The stress—strain relation is obtained as

$$\sigma = E_e\varepsilon_E = E_e(\varepsilon - \alpha_1 - \bar{\alpha}\Delta T) \quad (20)$$

Substitution of Eqn. (17) and (19) into the energy balance Eqn. (11) results in the coupled thermal-mechanical formula:

$$[(E_e\varepsilon - E_e\alpha_1 + E_e\bar{\alpha}T_0)\frac{d\alpha_1}{dt}] - [E_e\bar{\alpha}T\frac{d\varepsilon}{dt} + \rho c_V\frac{dT}{dt}] + k\frac{\partial^2 T}{\partial x^2} - h\frac{p}{A}(T - T_r) - \frac{p}{A}GFs(T^4 - T_r^4) = 0 \quad (21)$$

The terms in the first bracket arise due to the inelastic response, and the terms in the second bracket are the classical thermoelastic coupling terms for an adiabatic condition[13].

5.2 Additional constitutive assumptions

Based on the previous experimental characterization, the high-cycle fatigue process of ULTIMET alloy could induce thermodynamically and geometrically irreversible plastic strains and thermodynamically irreversible but geometrically reversible anelastic strains, as well as reversible elastic strains. As exhibited in Fig. 6(a), the walking distance between any two consecutive cycles is the thermodynamically and geometrically irreversible plastic strain, since the amount of plasticity due to the tensile stress was not opposed by an equal amount of the plastic flow in the compression direction. As fatigue progressed, due to strain hardening, the stress—strain responses would be expected to become elastic. However, due to fatigue damage, the stress—strain responses showed a linear viscoelastic behavior. As presented in Fig. 6 (b), during the loading and unloading process, the stress and strain can return to their initial stages, and the hysteresis loop is a closed loop at a later stage of cyclic loading. The anelastic behavior is geometrically reversible, but thermodynamically irreversible due to the energy loss of the hysteresis loop.

The exhibited viscoelastic behavior resulted from fatigue damage is assumed to be understood as a classical linear Kelvin-Voigt model. The constraint conditions implied by the Kelvin-Voigt model are

$$\frac{d\varepsilon}{dt} = \frac{d\varepsilon_E}{dt} + \frac{d\alpha_1}{dt} + \bar{\alpha}\frac{dT}{dt} \quad (22)$$

$$\sigma = \eta\frac{d\varepsilon_E}{dt} + E_a\varepsilon_E \quad (23)$$

where E_a is the elastic modulus, and η is the viscosity coefficient.

With the comparison of Eqns. (20) and (23), the effective elastic modulus, E_e, can be represented in the form of

$$E_e = E_a + \frac{\eta}{\varepsilon_E}\frac{d\varepsilon_E}{dt} \quad (24)$$

The thermal-mechanical response of the uniaxial bar subjected to uniaxial homogeneous high-cycle fatigue can be characterized using Eqns. (12) to (16) and (20) to (23).

However, for the low-cycle fatigue of ULTIMET alloy, the thermodynamically and geometrically irreversible plastic strains and reversible elastic strains are of main interest. In addition, the tests were conducted under constant strain rate control. Hence, Eqns. (19) and (20) could be used to describe the stress and strain behavior. The thermal-mechanical response of the uniaxial bar subjected to uniaxial homogeneous low-cycle fatigue can be characterized using Eqns. (20) and (21) together with Eqns. (12) to (16).

5.3 Numerical simulation

In order to implement the formulated model to predict the thermal and mechanical responses of the high-cycle fatigue of the material, the material constants of ULTIMET alloy are obtained from the manufacturing brochure as[32]

Elastic modulus $E = 238\,000$ MPa

Thermal expansion coefficient

$\bar{\alpha} = 13.0 \times 10^{-2}\ K^{-1}$

Density $\rho = 8\,470\ kg/m^3$

Specific heat at a constant volume

$c_V = 456\ J/(kg \cdot K)$

Convection heat transfer coefficient

$h = 12.5\ W/(m^2 \cdot K)$

Geometric factor $G = 1$

Emissivity $F = 1$

Stefan-Boltzmann constant

$s = 5.67 \times 10^{-8}\ W/(m^2 \cdot K^4)$

Note that the specific heat at a constant volume was chosen as the value of the specific heat at a constant pressure. In addition, the radii of the cylindrical bar, R, were 2.54 mm for high-cycle fatigue, and 3.81 mm for low-cycle fatigue.

Methods to obtain the material parameters for the Bonder-Partom's constitutive equations, Z_0, Z_1, Z_2, D_0, n, m_1 m_2 and m_3, were discussed by various authors[35~41]. The method by Chan et al[37, 38] was used herein. Their procedure had its basis in physical and phenomenological considerations and involved fitting the model parameters to the experimental data. By numerically integrating the coupled Eqns. (12) to (16) and (20) with the model parameters experimentally determined, and comparing the experimental tensile-test results with predicted ones, the material parameters of the model are refined to best fit the experimental stress—strain curves. The effective elastic modulus is equal to the elastic modulus of ULTIMET superalloy. The obtained parameters are shown in Table 2.

Table 2 Model parameters for ULTIMET alloy subjected to high-cycle fatigue

Z_0/MPa	Z_1/MPa	Z_2/MPa	D_0/s^{-1}
2 550	3 100	60	10^4
n	m_1/MPa^{-1}	m_2/MPa^{-1}	m_3/MPa^{-1}
1.085	0.15	5.44	0

Fig. 10 shows the experimental monotonic stress—strain curves, and those generated by the constitutive model with the above material parameters. At the strain rate of $5 \times 10^{-4}\ s^{-1}$, the experimental stress—strain curve of ULTIMET superalloy showed that the material was initially elastically deformed, then yielded and plastically deformed. With the strain rates of $0.001\ s^{-1}$ and $0.01\ s^{-1}$, the

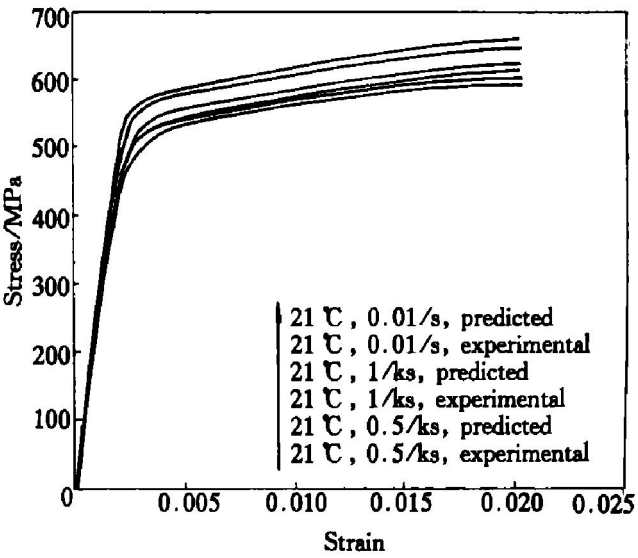

Fig. 10 Experimental and predicted stress—strain curves for tension tests of ULTIMET alloy at different strain rates

elastic and strain-hardening behavior shown in the experimental curve was not significantly different, but the yield point was raised to higher values. The predicted stress—strain curves displayed similar trends as the experimental ones at all three strain rates. The good agreement of the experimental and predicted results at $5 \times 10^{-4}\ s^{-1}$, $0.001\ s^{-1}$, and $0.01\ s^{-1}$. in Fig. 10 demonstrated the ability of the model to simulate the strain-rate effect.

To illustrate the stress—strain behavior and resulting temperature rise, an example is considered for a round bar subjected to high-cycle fatigue with an R ratio of 0.05, a maximum applied stress level of 703 MPa, and a reference temperature at 295.60 K, the same as the initial temperature of the specimen and the temperature of the environment. The stress—strain and thermal responses for the described condition can be obtained through the integration of Eqns. (12) to (16) and (20) to (23). The numerical simulation is fulfilled using a numerical integration scheme. To fit the stabilized hysteresis loop, the viscosity coefficient, η, is postulated to be small, as 0.1 GPa·s. The inputs of the model require the applied stress during fatigue, Fig. 11(a), the material constants, E, $\bar{\alpha}$, ρ, c_V, η, h, R, G, F, and s, and the parameters of Z_0, Z_1, Z_2, D_0, m_1, m_2, m_3, and n, as shown in Table 2.

The experimental and predicted temperature oscillations of ULTIMET alloy at the initial stage of high-cycle fatigue are shown in Fig. 11(b). In Fig. 11(b), the predicted temperature oscillations included heat conduction, convection, and radiation. It can be seen that, the present constitutive model was capable of predicting the complex temperature change resulting from cyclic fatigue. In the time region I of Fig. 11(b), the initial temperature decreased due to the thermoelastic effect as described by Eqn. (2).

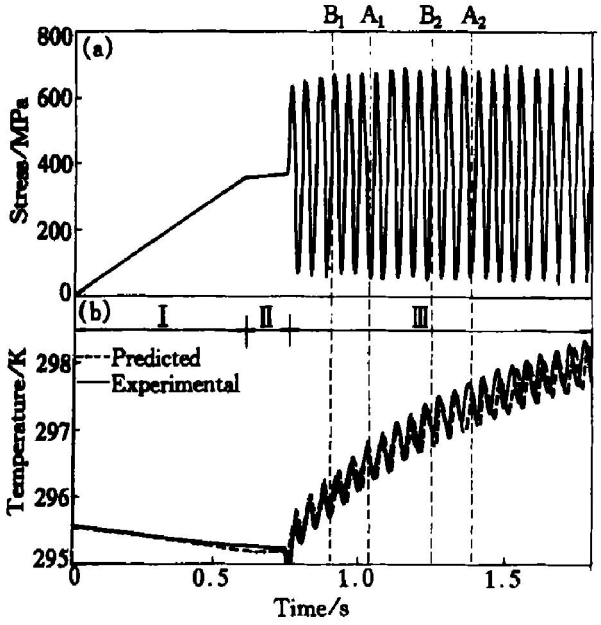

Fig. 11 Experimental and predicted temperature oscillations for ULTIMET alloy at initial cycles during high-cycle fatigue
(a) —MTS system command stress curve;
(b) —Corresponding temperature oscillations
(σ_{max} = 703 MPa, R = 0.05, room temperature, in air, fatigue life of 97 542 cycles and 20 Hz)

After the initial decrease, the temperature stayed constant in the time region II of Fig. 11(b), corresponding to the holding stage of the applied stress in Fig. 11(a). The temperature continued to decrease until the applied stress level was greater than the yield strength of the material. The temperature then increased sharply, which is due to the relatively large plastic deformation, as shown in Fig. 11(b). When the specimen was unloaded, the temperature continued to increase until the beginning of the second cycle. Thereafter, the temperature oscillated around an increasing mean temperature. As indicated by the dashed lines, A_1 and A_2, in Fig. 11, the highest temperature was always coincident with the lowest stress level. However, the lowest temperature did not concur with the highest stress level, as shown by the dashed lines, B_1 and B_2.

The experimental and predicted cyclic stress—strain curves are shown in Fig. 12. The predicted and experimental cyclic stress—strain curves are in reasonably good agreement. It can be seen that ULTIMET alloy experienced strain ratcheting, and eventually the strain stabilized with the typical shape in Fig. 6(b).

Since the cyclic loading was relatively fast, and the heat-transfer effect was relatively small, the testing condition could be regard as adiabatic. Especially, at the initial stage of fatigue cycling, there is no significant difference between the predicted temperatures in the consideration of insulated condition, only heat conduction, both heat conduction and convection, and the combination of heat conduction, convection,

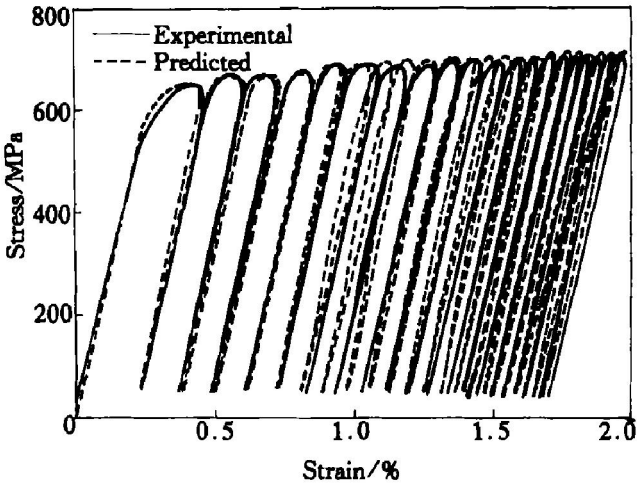

Fig. 12 Experimental and predicted cyclic stress—strain curves of ULTIMET alloy at initial cycles
(σ_{max} = 703 MPa, R = 0.05, room temperature, in air, fatigue life of 97 542 cycles and 20 Hz)

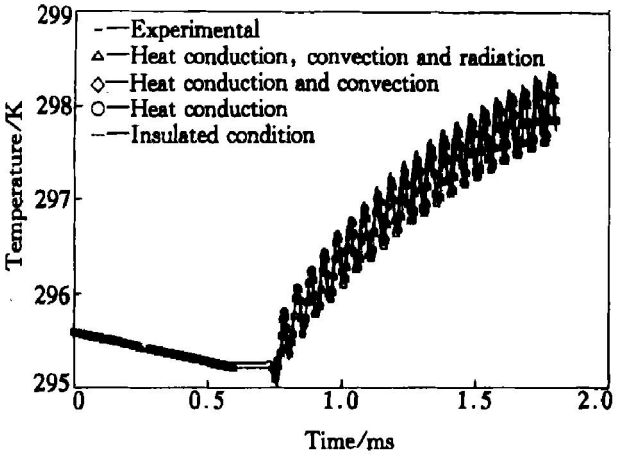

Fig. 13 Experimental and predicted temperature oscillations with consideration of insulated condition, only heat conduction, convection, and radiation, for ULTIMET alloy at initial cycles high-cycle fatigue
(σ_{max} = 703 MPa, R = 0.05, room temperature, in air, fatigue life of 97 542 cycles and 20 Hz)

and radiation, as shown in Fig. 13. The predicted temperatures based on the above different boundary conditions were in good agreement with the experimental one.

6 CONCLUSIONS

1) The thermography technique was capable of characterizing the delicate change of the specimen temperature during fatigue. It provided a new way to analyze the fatigue process.

2) The temperature profiles during high-cycle fatigue showed a characteristic trend, which could be categorized into four stages: the initial raise, steady state, abrupt increase, and final drop.

3) The increment of the mean temperature during fatigue testing was mainly due to inelastic defor-

mation. The oscillation of temperature was caused by the thermoelastic effect.

4) A constitutive model was developed for predicting the thermomechanical behavior of ULTIMET alloy subjected to cyclic fatigue. The constitutive model provided a better understanding of the thermal and mechanical responses of the alloy undergoing fatigue. The experimental and predicted results on temperature evolution and stress—strain responses were in good agreement for high-cycle fatigue.

5) The modified Bonder and Partom's constitutive equations was adequate to characterize plastic deformation during high-cycle fatigue.

ACKNOWLEDGEMENTS

Haynes International Inc. provided the major funding for this research project. It is gratefully acknowledged that the financial support of the National Science Foundation (NSF), the Division of Design, Manufacture, and Industrial Innovation, under Grant No. DMI-9724476, the Combined Research-Curriculum Development (CRCD) Program, under EEC-9527527, and the Integrative Graduate Education and Research Training (IGERT) Program, under DGE-9987548, to the University of Tennessee (UT), Knoxville, with Dr. D. Durham, Ms. M. Poats, Dr. W. Jennings, and Dr. L. Goldberg as the contract monitors. This research was also financially made possible by the U.S. Department of Energy, Assistant Secretary for Energy Efficiency and Renewable Energy, Office of Transportation Technologies, as part of the High Temperature Materials Laboratory (HTML) User Program under contract DE-AC05-96OR22464, managed by UT-Battelle LLC. In addition, appreciation goes to the financial support of the Center for Materials Processing and Office of Research Administration at UT, and the Southeastern Universities Research Association, with Dr. C. McHargue, Dr. K. Walker, and Dr. T. Hutchinson as the directors, respectively. We very much appreciate Mr. Yulin Lu's help in preparing the paper.

[REFERENCES]

[1] Wang H, Jiang L, Brooks C R, et al. Infrared temperature mapping of ULTIMET alloy during high-cycle fatigue [J]. Metallurgical and Materials Transaction A, 2000, 31A: 1307- 1310.

[2] Liaw P K, Wang H, Jiang L, et al. Thermographic detection of fatigue damage of pressure vessel steels at 1 000 Hz and 20 Hz [J]. Scripta Materials, 2000, 42: 389- 395.

[3] Blotny R, Kaleta K, Grzebien W, et al. A method for determining the heat energy of fatigue process in metals under uniaxial stress [J]. International Journal of Fatigue, 1986, 8(1): 35- 38.

[4] Sandor B I, Lohr D T, Schmid K C. Nondestructive testing using differential infrared thermography [J]. Materials Evaluation, 1987, 45(4): 382- 395.

[5] Attermo R, Ostberg G. Measurements of the temperature rise ahead of a fatigue crack [J]. International Journal of Fracture Mechanics, 1971, 7: 122- 124.

[6] Lohr D T, Enke N F, Sandor B I. Analysis of fatigue damage evolution by differential infrared thermography [A]. Proceedings of the 1987 SEM Fall Conference [C]. Savannah, Georgia, 1987. 139- 174.

[7] Gross T. Calorimetric measurement of the plastic work of fatigue crack propagation in quenched and tempered 4140 steel [D]. Northwestern University, Evanston, IL, 1981.

[8] Luong M P. Infrared thermographic scanning of fatigue in metals [J]. Nuclear Engineering and Design, 1995, 158: 363- 376.

[9] Luong M P. Fatigue limit evaluation of metals using an infrared thermographic technique [J]. Mechanics of Materials, 1998, 28: 155- 163.

[10] Charles J A, Appl F J, Francis J E. Thermographic determination of fatigue damage [J]. Transactions of ASME, 1978, 100(4): 200- 203.

[11] Huang Y, Li S X, Lin S E, et al. Using the method of infrared sensing for monitoring fatigue process of metals [J]. Materials Evaluation, 1984, 42(7): 1020- 1024.

[12] Coleman D, Gurtin M E. Thermodynamics with internal state variables [J]. Journal of Chemical Physics, 1967, 47(2): 597- 613.

[13] Stanley P, Chan W K. Quantitative stress analysis by means of the thermoelastic effect [J]. Journal of Strain Analysis, 1985, 20(3): 129- 137.

[14] Sandor B I, Lohr D T, Schmid K C. Nondestructive testing using differential infrared thermography [J]. Materials Evaluation, 1987, 45(4): 392- 395.

[15] Offermann S, Beaudoin J L, Bissieus C, et al. Thermoelastic stress analysis under nonadiabatic conditions [J]. Experimental Mechanics, 1997, 37(4): 409- 413.

[16] Suresh S. Fatigue of Materials, 2nd ed [M]. Cambridge, Great Britain at the University Press, 1998.

[17] Puskar A, Golovin S A. Fatigue in Materials: Cumulative Damage Processes [M]. Amsterdam, Elsevier Science Publishers, 1985.

[18] Halford G R. Stored energy of cold work changes induced by cyclic deformation [D]. University of Illinois, Urbana, IL, 1966.

[19] Liaw P K, Kwun S I, Fine M E. Plastic work of fatigue crack propagation in steels and aluminum alloys [J]. Metallurgical Transactions, 1981, 12A: 49- 55.

[20] Fine M E, Davidson D L. Fatigue Mechanisms, Advances in Quantitative Measurement of Physical Damage [M]. ASTM STP 811, American Society for Testing and Materials, 1983. 350- 370.

[21] Chaboche J L. Unified Cyclic Viscoplastic Constitutive Equations: Development, Capabilities, and Thermodynamic Framework [M]. Unified Constitutive Laws of Plastic Deformation, Krausz A S, Krausz K, eds. Academic Press, Inc, 1996. 1- 68.

[22] Kratochvil J, Dillon O W. Thermodynamics of elastic-plastic materials as a theory with internal state variables [J]. Journal of Applied Physics, 1969, 40(8): 3207- 3218.

[23] Dillon O W. Coupled thermoplasticity [J]. Journal of Mechanics and Physics in Solids, 1963, 11: 21- 23.

[24] Kratochvil J, Dillon O W. Thermodynamics of crys-

talline elastic-visco-plastic materials [J]. Journal of Applied Physics, 1970, 41(4): 1470- 1479.
[25] Cernocky E P, Krempl E. A coupled isotropic theory of thermoviscoplasticity and its prediction for stress and strain controlled loading in torsion [A]. Thermal Stresses in Severe Environments, 1980, Blacksburg, Virginia, pp. 47- 60.
[26] Liu M C M, Krempl E. A uniaxial viscoplastic model based on total strain and overstress [J]. Journal of Mechanics and Physics in Solids, 1979, 27: 377- 391.
[27] Cernocky E P, Krempl E. A nonr-linear uniaxial integral constitutive equation incorporating rate effects, creep and relaxation [J]. Journal of Nonr-Linear Mechanics, 1979, 14: 183- 203.
[28] Cernocky E P, Krempl E. A theory of thermoviscoplasticity based on infinitesimal total strain [J]. International Journal of Solids Structures, 1980, 16: 723- 741.
[29] Allen H, Haisler W E. A theory for analysis of thermoplastic materials [J]. Mechanics and Structures, 1981, 13: 129- 135.
[30] Allen H. A prediction of heat generation in a thermoviscoplastic uniaxial bar [J]. International Journal of Solids Structures, 1985, 21(4): 325- 342.
[31] Hart E W. Constitutive relations for the nonelastic deformation of metals [J]. Journal of Engineering Materials and Technology, 1976(7): 193- 202.
[32] ASTM (American Society for Testing and Materials). Standard Practice (E466). Conducting Constant Amplitude Axial Fatigue Tests of Metallic Materials [S]. 1995.
[33] ASTM (American Society for Testing and Materials). Standard Practice (E606). Strain Controlled Fatigue Testing [S]. 1995.
[34] Brown L M, Ogin S L. Fundamentals of deformation and fracture [A]. Proceedings of the Eshelby Memorial Symposium [C]. 1984. 500- 528.
[35] Bodner S R, Partom I, Partom Y. Uniaxial cyclic loading of elastic viscoplastic materials [J]. Journal of Applied Mechanics, 1979, 46(12): 805- 810.
[36] Bodner S R, Partom Y. Constitutive equations for elastic-viscoplastic strain-hardening materials [J]. Journal of Applied Mechanics, 1975, 42(2): 385- 389.
[37] Chan K S, Bonder S R, Lindholm U S. Phenomenological modeling of hardening and thermal recovery in metals [J]. Journal of Engineering Materials and Technology, 1988, 110: 1- 8.
[38] Chan K S, Lindholm U S, Bonder S R, et al. High temperature inelastic deformation under uniaxial loading: theory and experiment [J]. Journal of Engineering Materials and Technology, 1989, 111: 345- 353.
[39] Rowley M A, Thornton E A. Constitutive modeling of the visco-plastic response of hastelloy-X and Aluminum Alloy 8009 [J]. Journal of Engineering Materials and Technology, 1996, 118: 19- 27.
[40] Li K, Jr Sharpe W N. Viscoplastic behavior of a notch root at 650C: ISDG Measurement and Finite Element Modeling [J]. Journal of Engineering Materials and Technology, 1996, 118: 88- 93.
[41] Skipor A F, Harren S V, Botsis J. On the constitutive response of 63/37 Sn/Pb eutectic solder [J]. Journal of Engineering Materials and Technology, 1996, 118: 1- 11.

(Edited by YANG Bing)